

# Do It Yourself Hyperspectral Imaging with Everyday Digital Cameras

Seoung Wug Oh<sup>1</sup>   Michael S. Brown<sup>2</sup>   Marc Pollefeys<sup>3</sup>   Seon Joo Kim<sup>1</sup>  
<sup>1</sup>Yonsei University   <sup>2</sup>National University of Singapore   <sup>3</sup>ETH Zurich

## Abstract

Capturing hyperspectral images requires expensive and specialized hardware that is not readily accessible to most users. Digital cameras, on the other hand, are significantly cheaper in comparison and can be easily purchased and used. In this paper, we present a framework for reconstructing hyperspectral images by using multiple consumer-level digital cameras. Our approach works by exploiting the different spectral sensitivities of different camera sensors. In particular, due to the differences in spectral sensitivities of the cameras, different cameras yield different RGB measurements for the same spectral signal. We introduce an algorithm that is able to combine and convert these different RGB measurements into a single hyperspectral image for both indoor and outdoor scenes. This camera-based approach allows hyperspectral imaging at a fraction of the cost of most existing hyperspectral hardware. We validate the accuracy of our reconstruction against ground truth hyperspectral images (using both synthetic and real cases) and show its usage on relighting applications.

## 1. Introduction

Color is the visual perception or interpretation of light. Light is a continuous electromagnetic radiation over a range of spectrum (visible light ranges from 400nm to 700nm). The human vision system, as well as most cameras, sense this physical light through a tri-stimulus mechanism where three channels respond differently to the incoming light as follows:

$$p_k = \int_{\Omega} o(\lambda)c_k(\lambda)d\lambda, \quad (1)$$

where  $p_k$  is the output of the  $k^{th}$  channel,  $\Omega$  is the range of the visible spectrum,  $o$  is the incoming light, and  $c_k$  represents the spectral response of the  $k^{th}$  sensor channel. For the vast majority of cameras, these three channels have spectral sensitivity that fall into the red, green, and blue ranges of the visible spectrum.

While this three channel tri-stimulus representation is good for representing perceived color, it falls short of ex-

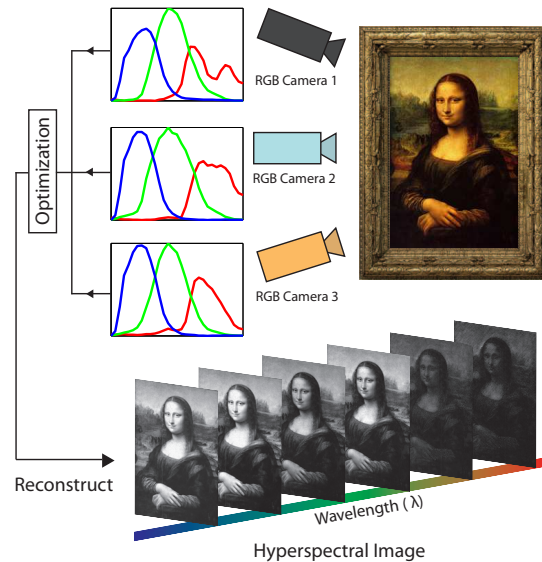


Figure 1. This image shows an overview of our system. We reconstruct hyperspectral images by capturing images of a scene with multiple consumer cameras. Our system exploits the different spectral sensitivities of different cameras and convert their different color measurements into hyperspectral signals.

plaining the full physical nature of light. For example, when different cameras are used, the same light spectral power distribution may result in different colors due to the different spectral responses  $c_k$  of the cameras. In addition, two distinct spectral power distributions may result in the same R, G, B values on the same camera due to projection of the light onto only three color channels. Hyperspectral imaging (HSI), on the other hand, records a more accurate representation of physical light as it captures dense spectral samples across the visible wave lengths. The difference between multispectral imaging and hyperspectral imaging is the number of bands captured. Multispectral imaging generally captures a small number of bands (3 to 10 channels), while hyperspectral imaging usually records higher number of channels. We refer to our approach as hyperspectral imaging as our goal is to sample the visible spectrum with

31 channels (every 10nm between 400nm and 700nm).

Due to the physical nature of hyperspectral data, HSI has been effectively used for different applications that require accurate measurements of light. For example, HSI has been used for cultural heritage analysis to record the spectral data of historical documents and paintings [10, 19, 29]. HSI has also been widely used for scientific applications such as earth science and remote sensing [9, 23], astronomy [22], medical science, food science [24, 27] and computer vision [30].

The most significant drawback for working with hyperspectral imaging is obtaining access to a hardware that is able to densely sample the visible spectra. Hyperspectral imaging devices typically have costs in the range of tens of thousands of dollars. Not surprisingly, only a handful of researchers have access to such equipment. This is evident in the small number of datasets that are currently available [5, 14, 35]. There has been recent work that has exploited active illumination to build HSI systems [6, 31]. These methods multiplex varying illumination into a scene to recover the hyperspectral reflectance of objects. While such methods are more affordable, this type of HSI system requires a significant amount of expertise to build the necessary illumination infrastructure. In addition, such systems cannot be used outdoors as they rely on controlling the illumination in the scene.

**Contribution** In this paper, we propose a novel algorithm to reconstruct a hyperspectral image of a scene from multiple images taken by different consumer cameras (Fig. 1). In particular, we propose an algorithm that uses the different spectral sensitivities of the different cameras to reconstruct the hyperspectral signal at different scene points. We cast this as an optimization problem that simultaneously estimates a bilinear system that models the spectral reflectance of scene points as well as the illumination spectrum. Our work leverages priors on the space of camera spectral sensitivities as well as the space of real world material and illumination. We describe an effective alternating-optimization framework that can solve this bilinear system and produce a high-quality hyperspectral image for both indoor and outdoor scenes. This overall framework and corresponding optimization algorithm enables an affordable and easy to use system for hyperspectral imaging.

The remainder of this paper is organized as follows: Section 2 describes related work; Section 3 provides the details of our HSI framework including the problem formulation, analysis of camera spectral sensitivities, and proposed optimization approach; Section 4 demonstrates a number of experiments on synthetic and real data. This is followed by a discussion in Section 5.

## 2. Related Work

Most commercial systems for HSI provide hardware that captures a large number of images with a tunable narrow band filter [12]. Multiple images are taken with a spectral filter that only allows spectral energy at a certain wavelength to pass through the filter. This process is repeated for a set discrete of wavelengths. A HSI system that provides 31 bands (every 10nm between 400nm and 700nm) would need to take 31 images, each image with different spectral filter. Another commercial option is to employ a pushbroom imaging framework to reconstruct the spectrum column by column [21]. In these systems, a column of light enters the camera and is passed through a prism or a diffraction grid to decompose the light into its individual wavelengths that is then recorded by the camera sensor. The full hyperspectral image is reconstructed by filling each line by rotating the camera. While commercial hyperspectral cameras provide accurate spectral measurements, the hardware requires careful control of mechanical components that significantly increase the cost of the equipment. Another problem is that the image resolutions for these systems are often low compared to conventional cameras, so super-resolution algorithms may be necessary to increase the resolution as described in [17].

There have been a number of works that propose alternatives to tunable filters or push-broom designs. For example, the work in [31] reconstructed a multispectral video from RGB images by capturing a scene under a set of light sources with different spectral power distributions. The key component of their system is a technique to determine the optimal multiplexing sequence of spectral sources in order to minimize the number of required images for HSI. The work in [6] also took advantage of active lighting by using an optimized wide band illumination to obtain multispectral reflectance information. Instead of putting the spectral filters in front of the camera itself, the key idea of the work in [6] is to put the spectral filters in front of the illumination. While these active illumination methods provide an effective means for HSI, they do require expertise to build and use. Another major limitation is that they can only be used indoors under controlled lighting conditions.

Instead of using active illuminations, fast algorithms for multispectral video capture were proposed by using a prism in [11] and a DLP projector in [13]. In [11], a prism was used to separate the incoming light's spectra. An optical mask was placed in front to avoid overlap between neighboring rays that would make the boundaries between the different pixel's spectra ambiguous. A unique color-forming mechanism via DLP projectors combined with a high speed camera was exploited for spectral reflectance recovery in [13]. A common difficulty in using these systems is expertise necessary to set up the required hardware systems.

Single image multispectral imaging algorithms have also been proposed. Since an RGB camera provides three measurements per pixel only, it is an ill-posed problem to recover the higher dimensional signal per pixel directly from a single image. Single image methods therefore need to impose strong assumptions on the surface reflectance and rely extensively on associated training data to constrain the solution. To model the mapping from an RGB signal to higher dimensional spectral signal, prior single image methods have performed reconstruction using a metamer-set [26], or reconstruction using linear [1] and non-linear [28] interpolation using the associated training data. The results of these methods depend highly on the training data and their similarity to the imaged scene.

Compared to the aforementioned methods, the HSI method proposed in this paper offers several advantages. First, we only require the use of multiple commodity cameras; special filters, lights, etc., are not required. This makes the system relatively low-cost and easy to use. Our approach is also able to recover hyperspectral images much more accurately as compared to single image based methods. In addition, by using commodity cameras, our method inherently provides high resolution hyperspectral images. Since we simultaneously recover both the surface spectra and the illumination spectra, an extra stage for light separation as performed in [18] is unnecessary. Lastly, our system can be used both indoors and outdoors.

### 3. HSI Algorithm

#### 3.1. Problem Formation

We first introduce the imaging model of digital RGB cameras. We assume Lambertian surface with a uniform illumination for the whole scene, and also assume that images for different cameras were taken under the same lighting condition. Another important assumption for this work is that the spectral sensitivities (or camera responses) for the cameras are known. A pixel intensity of an image from  $m^{th}$  camera can be expressed as:

$$p_{m,k}(x) = \int_{\Omega} s(\lambda, x) l(\lambda) c_{m,k}(\lambda) d\lambda, \quad (2)$$

where  $p_{m,k}(x)$  is the intensity of a pixel  $x$  in the  $k^{th}$  channel of the image from the  $m^{th}$  camera,  $\Omega$  is the range of the visible spectrum,  $s(\lambda, x)$  is the spectral reflectance of the scene point  $x$ ,  $l(\lambda)$  is the spectral power distribution of the illumination, and  $c_{m,k}(\lambda)$  is the spectral sensitivity of  $m$ -th camera for the  $k^{th}$  channel.

It is widely known that surface spectral reflectance of real-world materials can be well approximated using a linear combination of a small number of spectral basis [7, 25, 32]:

$$s(\lambda, x) = \sum_{i=1}^{N_r} r_i(x) b_i(\lambda), \quad (3)$$

where  $N_r$  is the number of the reflectance basis,  $b_i(\lambda)$  is the basis function of the spectral reflectance, and  $r_i(x)$  is the corresponding coefficient for the  $i^{th}$  basis. In this work, we compute the basis functions  $b_i(\lambda)$  by running Principal Component Analysis (PCA) on the dataset that contains the measurement of spectral reflectance of 1257 Munsell color chips [32]. The number of basis was set to 8 (i.e.  $N_r = 8$ ), which is able to explain more than 99% of the total variance of the data.

We model the illumination  $l(\lambda)$  in a similar fashion as the spectral power distributions of real-world illumination is also known to lie in a low dimensional space [16, 33]. This can be expressed as:

$$l(\lambda) = \sum_{j=1}^{N_a} a_j e_j(\lambda), \quad (4)$$

where  $N_a$  is the number of illuminant basis,  $e_j(\lambda)$  is a basis function for illuminant spectra, and  $a_j$  is the corresponding coefficient. To compute the basis functions, we use the database from [3] which contains spectra of 102 illuminations. We perform PCA separately on the outdoor and indoor illuminants. We use 65 illuminants for outdoor scenes and use all 102 illumination for indoor scenes. The number of basis,  $N_a$ , is set to 4 for outdoors, and 6 for indoors.

Combining our models for surface reflectance and scene illumination, we can rewrite Eq. 2 to obtain:

$$\begin{aligned} p_{m,k}(x) &= \sum_{i=1}^{N_r} \sum_{j=1}^{N_a} r_i(x) a_j \int_{\Omega} b_i(\lambda) e_j(\lambda) c_{m,k}(\lambda) d\lambda \\ &= \sum_{i=1}^{N_r} \sum_{j=1}^{N_a} r_i(x) a_j \mathbf{A}_{m,k}(i, j), \end{aligned} \quad (5)$$

where  $\mathbf{A}_{m,k}(i, j) = \int b_i(\lambda) e_j(\lambda) c_{m,k}(\lambda) d\lambda$ .

The above equation can be expressed in a matrix format as:

$$p_{m,k}(x) = \mathbf{r}(x)^T \mathbf{A}_{m,k} \mathbf{a}, \quad (6)$$

where  $\mathbf{r}(x) = [r_1(x), r_2(x), \dots, r_{N_r}(x)]^T$ ,  $\mathbf{a} = [a_1, a_2, \dots, a_{N_a}]^T$ , and  $\mathbf{A}_{m,k}$  is a  $N_r \times N_a$  matrix.

For an image with  $n$  pixels, the intensity and the surface reflectance at every pixel can be rearranged to obtain:

$$\mathbf{p}_{m,k} = \mathbf{R}^T \mathbf{A}_{m,k} \mathbf{a}, \quad (7)$$

where  $\mathbf{p}_{m,k} = [p_{m,k}(1), p_{m,k}(2), \dots, p_{m,k}(n)]^T$  is the pixel intensity vector of length  $n$ , and  $\mathbf{R} = [\mathbf{r}(1), \mathbf{r}(2), \dots, \mathbf{r}(n)]$  is the  $N_r \times n$  surface reflectance matrix.

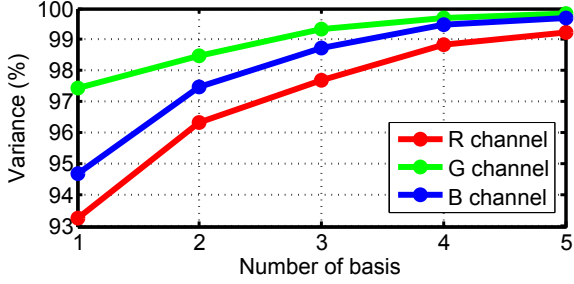


Figure 2. The percentage of the variance with growing number of basis for R,G,B channels separately. We can observe that the space is close to being 8D.

This bilinear system in Eq. 7 is the final formulation that forms the core of our spectral imaging system. The goal now is to compute both the surface reflectance  $\mathbf{R}$  and the illumination spectrum  $\mathbf{a}$  from multiple observations of the scene from different cameras. Using  $N_c$  number of cameras gives us  $N_c \times 3$  observations as each camera provides three color channels. It is important to note that the intensity values from cameras must be from camera RAW images as the values from regular JPEG images are heavily processed violating our imaging model [20]. We used the *dcrw* software to obtain linear RGB images from camera RAW data.

### 3.2. Analysis of the Spectral Sensitivities of Cameras

The premise of our work is that different cameras provide different samples of the spectrum to enable the full reconstruction of the spectrum when combined. This means the accuracy of the estimated hyperspectral signals obtained by solving Eq. 7 depends on the relationship between the spectral sensitivities of different cameras. The best scenario would arise when the spectral responses are narrow band in nature with no overlap between different cameras. The worst case would be when the spectral sensitivities of different camera models are almost identical.

We analyzed the spectral sensitivities of different cameras as done in [15, 18] to validate that they provide enough independent measurements of the incoming light spectrum. The space of the camera spectral response for each channel was reported to lie in two dimensional manifold in [15] and a three dimensional manifold in [18]. We combined the data provided in [15, 18] and performed PCA on a dataset of 40 cameras. The percentage of the variance with growing number of basis is plotted in Fig. 2. While the space of the spectral sensitivities is low, we can observe that they are close to being eight dimensional for all three channels together (e.g. two basis for the green, three basis for the red and the blue channels respectively). This eight dimensional basis provides enough variance to solve our problem in Eq. 7.

### 3.3. Optimization using Alternating Least Squares

The bilinear system in Eq. 7 can be solved by minimizing the following objective function in a least squares sense with respect to  $\mathbf{R}$  and  $\mathbf{a}$ :

$$\hat{\mathbf{R}}, \hat{\mathbf{a}} = \arg \min_{\mathbf{R}, \mathbf{a}} \sum_{m=1}^{N_c} \sum_{k=1}^3 |\mathbf{p}_{m,k} - \mathbf{R}^T \mathbf{A}_{m,k} \mathbf{a}|_2^2. \quad (8)$$

However, there are additional constraints we can place on the solution as follows:

$$\begin{aligned} \hat{\mathbf{R}}, \hat{\mathbf{a}} = \arg \min_{\mathbf{R}, \mathbf{a}} & \left\{ \sum_{m=1}^{N_c} \sum_{k=1}^3 |\mathbf{p}_{m,k} - \mathbf{R}^T \mathbf{A}_{m,k} \mathbf{a}|_2^2 \right. \\ & + \alpha \sum_{x=1}^n \int_{\Omega} \left( \frac{\partial^2 s(\lambda, x)}{\partial \lambda^2} \right)^2 d\lambda \\ & \left. + \beta \int_{\Omega} \left( \frac{\partial^2 l(\lambda)}{\partial \lambda^2} \right)^2 d\lambda \right\}, \end{aligned} \quad (9)$$

*s.t.*  $s(\lambda, x), l(\lambda) \geq 0$  for all  $\lambda, x$ .

In Eq. 9, we imposed an additional positivity constraints as both the surface and the illumination spectra should be positive. We also impose a smoothness constraint on both the surfaces and the illumination as this is often observed in real world surfaces and illumination spectra.

The objective function can be expressed in matrix form as follows:

$$\begin{aligned} \hat{\mathbf{R}}, \hat{\mathbf{a}} = \arg \min_{\mathbf{R}, \mathbf{a}} & \left\{ \sum_{m=1}^{N_c} \sum_{k=1}^3 |\mathbf{p}_{m,k} - \mathbf{R}^T \mathbf{A}_{m,k} \mathbf{a}|_2^2 \right. \\ & \left. + \alpha \|\mathbf{WBR}\|_F^2 + \beta \|\mathbf{WEa}\|_2^2 \right\}, \end{aligned} \quad (10)$$

*s.t.*  $\mathbf{BR}, \mathbf{Ea} \geq 0$ ,

where  $\mathbf{W}$  is the second-order difference matrix,  $\mathbf{B}_{v,i} = b_i(v)$  with  $i$  is from 1 to  $N_r$ ,  $\mathbf{E}_{v,j} = a_j(v)$  with  $j$  is from 1 to  $N_a$ , and  $v$  is from 1 to 31.  $v$  represents 31 bands from 400nm to 700nm with the intervals of 10nm.

A least squares solution for this system of bilinear equations can be found by iteratively solving the two linear sub-problems [2, 8]. To minimize Eq. 10, we adopt the alternating least squares method in [2] and alternate between solving for the illumination  $\mathbf{a}$  by fixing the surface reflectance  $\mathbf{R}$  and then solving for  $\mathbf{R}$  with fixed  $\mathbf{a}$ . We have empirically found that the initialization of  $\mathbf{R}$  does not significantly affect the results, and we initialize every spectral reflectance as the first reflectance basis. Details on the alternating least squares optimization steps are included in the supplementary material.

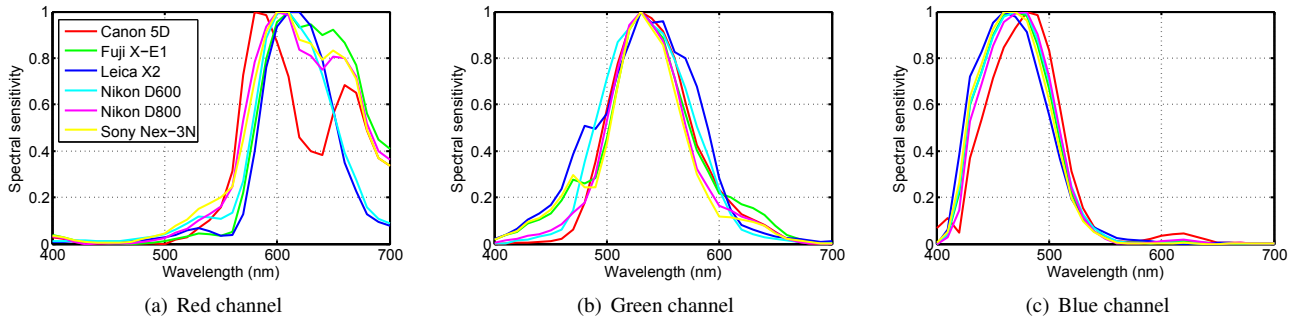


Figure 3. The spectral sensitivity of the 6 cameras used in this work (Canon 5D, Fujifilm X-E1, Leica X2, Nikon D600, Nikon D800, and Sony Nex-3N).

### 3.4. Hyperspectral Image Reconstruction

Our HSI framework relies on multiple observations from different cameras. To reconstruct a high resolution hyperspectral image, a registration process is necessary to find correspondences between images to build the observations vectors  $\mathbf{p}_{m,k}$  in Eq. 7. To allow us to focus on the HSI reconstruction, we captured planar scenes so that homographies could be used for the registration. Note that our hyperspectral imaging algorithm itself is general that can be used for non-planar scenes with a dense registration method such as dense stereo matching [34], patch-match [4], etc. While such registration is possible, it comes with its own challenges that is outside the scope of this paper.

Solving the bilinear system iteratively for all the pixels in the high resolution images can be extremely slow as the size of matrix  $\mathbf{R}$  grows with the number of pixels. For fast computation, we first solve Eq. 10 for a selected number of points (e.g. 30 points only). Since the solution provides the illumination spectrum  $\mathbf{a}$ , the rest of the surface reflectance spectra  $\mathbf{R}$  can now be solved linearly with the known illumination spectrum  $\mathbf{a}$ .

## 4. Experiments

### 4.1. Camera Spectral Sensitivity

Before running our algorithm to reconstruct hyperspectral images, we need to compute the spectral sensitivities of the cameras employed in our system. We used six cameras in this work as follows: Canon 5D, Fujifilm X-E1, Leica X2, Nikon D600, Nikon D800, and Sony Nex-3N. To estimate the spectral sensitivities, we measured the spectral signals of the Macbeth color chart and additional color chips using a hyperspectral camera (Specim PFD-V10E) and captured images of the same object with our 6 cameras at the same time. We perform PCA on the camera spectral sensitivity database from [15] and [18], and the first five basis functions were used for the estimation of the sensitivities. Spectral sensitivity  $\hat{\mathbf{c}}_k$  was computed by solving the follow-

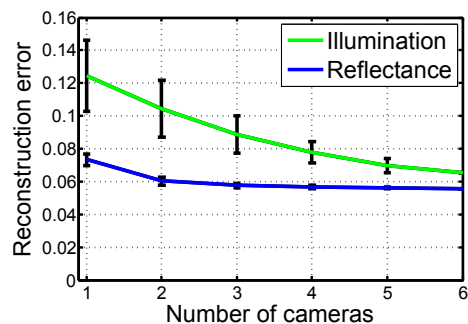


Figure 4. The average error for estimated reflectance and illumination according to the number of cameras used.

ing equation:

$$\hat{\mathbf{c}}_k = \mathbf{H}_k \hat{\mathbf{q}}_k, \quad (11)$$

where

$$\begin{aligned} \hat{\mathbf{q}}_k &= \arg \min_{\mathbf{q}_k} \|\mathbf{p}_k - \mathbf{D}\mathbf{H}_k \mathbf{q}_k\|_2^2, \\ s.t. \quad &\mathbf{H}_k \mathbf{q}_k \geq 0, \end{aligned} \quad (12)$$

where  $\mathbf{c}_k$  is camera spectral sensitivity of the  $k^{th}$  channel,  $\mathbf{H}_k$  is the matrix of the basis functions,  $\mathbf{q}_k$  is the corresponding coefficient vector,  $\mathbf{p}_k$  is the observed pixel intensity of color chart in channel  $k$ , and  $\mathbf{D}$  is the matrix of stacked color chart patches' hyperspectral signal. Fig. 3 shows the spectral sensitivities of our 6 cameras.

### 4.2. Experiments on Synthetic Data

We first perform experiments on synthetic data to validate our algorithm as well as to analyze the effect of the number and the selection of the cameras. Ground truth spectral reflectance of the Macbeth color chart patches and samples of illumination spectra from [3] were used to generate hyperspectral scenes of the Macbeth Chart. We then generated RGB values of each color patch for each camera according to Eq. 2 with the computed camera spectral sensitivities. While generating the RGB values, we added

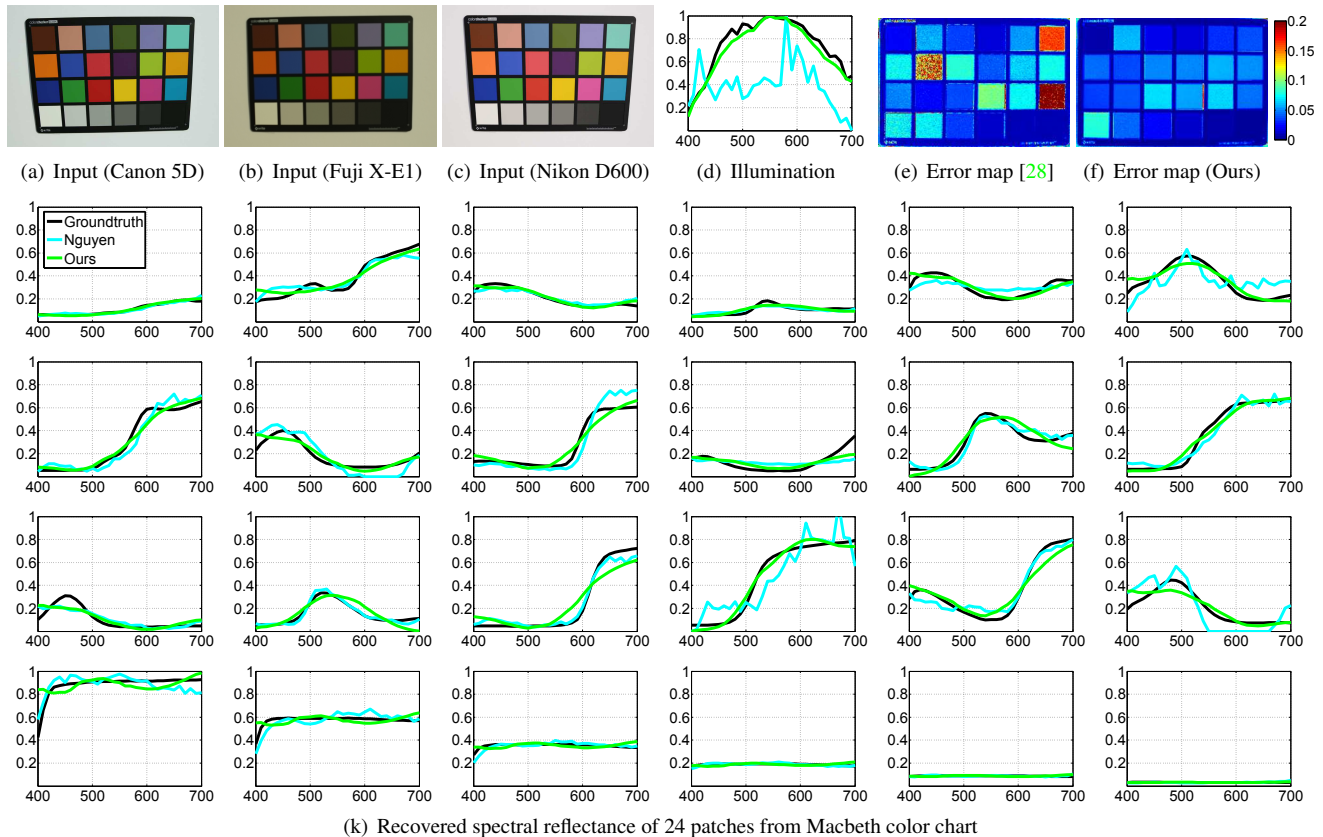


Figure 5. Outdoor experiment under sunlight using a Macbeth color chart. The results from our method and the single image based method [28] are compared. (a)-(c) RGB inputs from three different cameras, (d)-(f) estimated illumination spectrums and pixel-wise surface reflectance reconstruction error of Nguyen *et al.*'s method [28] and our method, (k) recovered surface spectral reflectance of 24 patches using the two methods.

zero mean Gaussian noise with a standard deviation of 15 to simulate noise as well as mis-registration between images.

Fig. 4 shows the root-mean-square-error (RMSE) for both the reconstructed color patches and the reconstructed illumination as the number of used cameras increases. To investigate the effect of the number of cameras, we test all 63 combinations of our cameras. The results in Fig. 4 report the average errors per number of cameras. As expected, using a single camera image is not sufficient, however, the reconstruction error begins to stabilize starting with two and more cameras (especially for the surface). The analysis shows that using three cameras would be good for both the effectiveness and the accuracy, and it also shows that using more than four cameras is not necessary as it does not increase the accuracy. This is expected as the space of the camera spectral sensitivity is low and this analysis also fits with our observation in Fig. 2.

With the above analysis, we fixed the number of cameras to be used as three. The criteria for finding the best combination of camera should depend on linear independence of the cameras spectral sensitivities. For camera selection, we build a matrix with columns being the spectral sensitivities

and chose the combination with the lowest condition number (the ratio between the maximum and the minimum singular values of the matrix). The combination of Canon 5D, Fuji X-E1, Nikon D600 cameras produced the lowest condition number and indeed resulted in the most accurate reconstruction. The following examples of real scenes were all conducted with the above combination.

### 4.3. Experiments on Real Data

For the experiments on real data, we captured hyperspectral images of several planar objects under different illumination with a hyperspectral camera as ground truth data. The same scenes are photographed using the selected three cameras. For the real data experiments, homographies from each image to the ground truth hyperspectral image are computed for the registration and the resolution of the examples in this paper is  $200 \times 300$  that covers a single planar object. With a Matlab implementation, it takes 2 minutes for our algorithm to reconstruct the hyperspectral image with that resolution.

Fig. 5 compares HSI results of our method and the single image based method in [28]. For this experiment, a

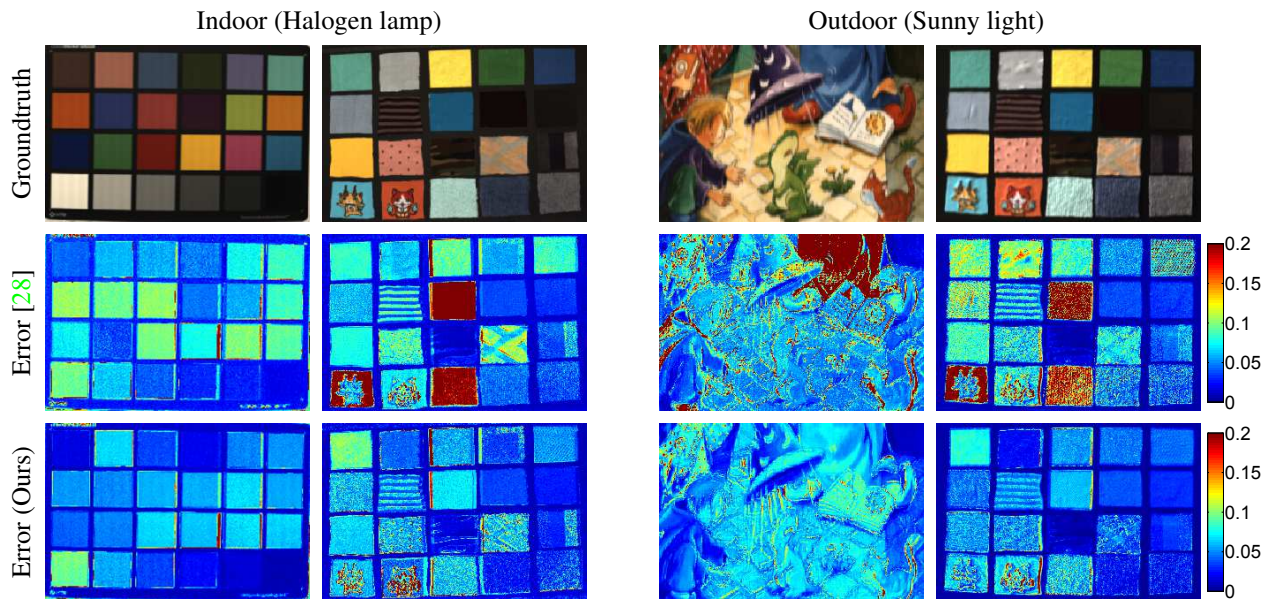


Figure 6. Hyperspectral imaging results of various planar scenes under indoor and outdoor illuminations. Results of our method and Nguyen *et al.*'s method [28] are compared. The ground truth spectral reflectance is rendered as RGB images using spectral sensitivities of a Canon 5D camera for reference. The errors indicate RMSE in the hyperspectral domain.

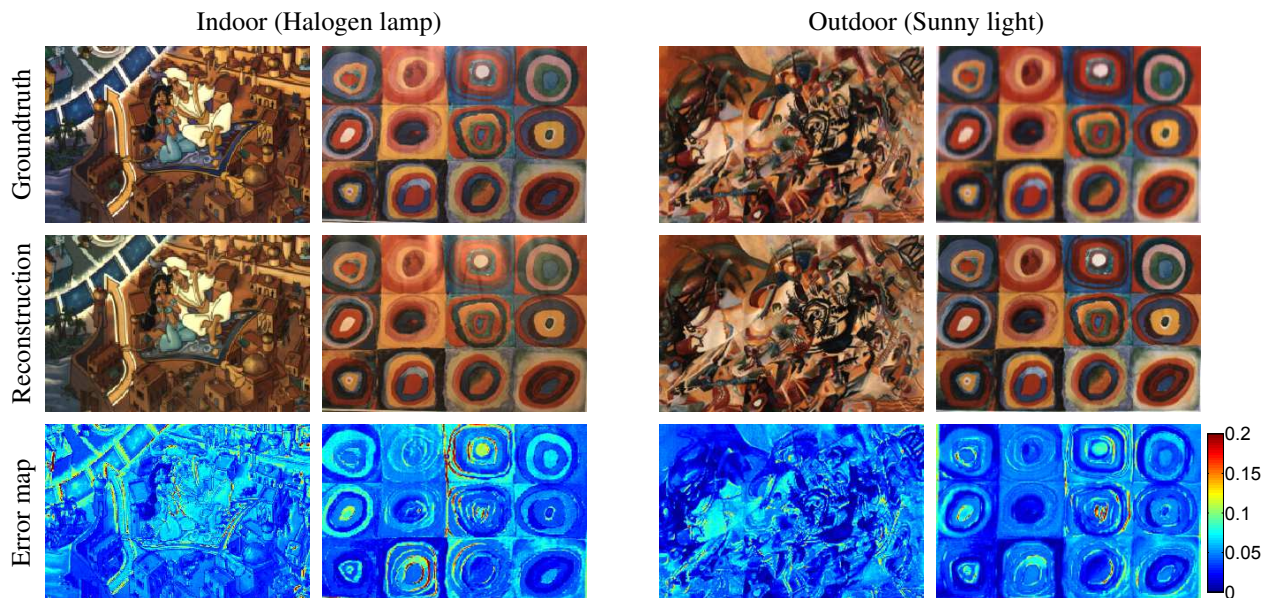


Figure 7. Recovered reflectance of paintings using the proposed method. RGB images of paintings taken under both indoor and outdoor lighting conditions are converted to hyperspectral images. The ground truth and the reconstructed hyperspectral images are rendered as RGB images using the spectral sensitivities of the Canon EOS-5D camera. The errors indicate RMSE in the hyperspectral domain.

Macbeth color chart was imaged outdoors under the sunlight. As can be seen, the hyperspectral signals of both the illumination and the patches recovered by our method are more accurate than the ones recovered by [28]. In addition to Fig. 5, results on more various scenes under both indoor and outdoor illuminations are shown in Fig. 6. The color in

the error maps indicates pixel-wise RMSE in the hyperspectral domain. The proposed method constantly outperforms the previous method that uses single RGB image [28] on various scenes and lighting conditions.

Fig. 7 shows reconstructed hyperspectral images of paintings under both indoor and outdoor illuminations.

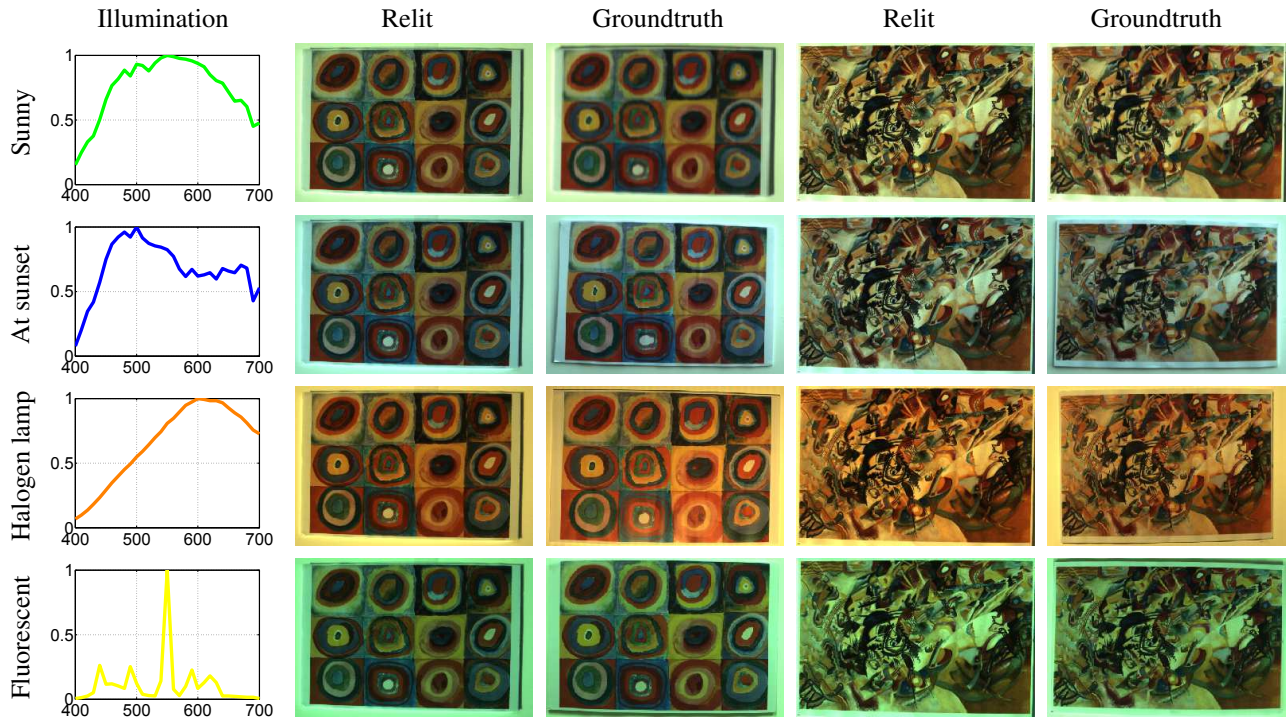


Figure 8. Relighting applications. Spectral surface reflectance estimated by our method are relit using 4 different illuminations and rendered as RGB images using the camera sensitivity of a Nikon D600 camera. The relighting results are compared with ground truth images: scenes taken under the specified illumination.

Both the ground truth and the reconstructed hyperspectral images are visualized as RGB color images. The reconstruction is satisfactory except for some edge regions, where the registration may not be accurate enough. The estimated spectral reflectance can be used to relight the scene. Fig. 8 illustrates the use of our method on relighting.

## 5. Discussion

We have introduced a framework for affordable and easy-to-use hyperspectral imaging using commercial digital cameras. Our system exploits the variation in the spectral sensitivities of cameras and combines the different color measurements into a full hyperspectral signal. We have demonstrated the effectiveness and the accuracy of our system using various examples both indoors and outdoors, and demonstrated the ability to use the hyperspectral data for tasks such as scene re-lighting.

While our system was able to reliably reconstruct hyperspectral images in most cases, it ran into a problem when the system was used under a fluorescent illumination. This is due to the rather peculiar spectrum of fluorescent lights as shown in the fourth example of Fig. 8. The energy is focused on a sparse set of spectral bands for this type of lighting and the variation of observations by different sensors become negligible for our system to work well.

There are several interesting directions for future work. From a practical viewpoint, we would like to extend the work to work with 3D scenes by applying dense stereo matching registration. With our framework and a 3D reconstruction system, we could generate 3D hyperspectral texture-maps. Additionally, we would like to remove the need to know the spectral sensitivities of the camera by incorporating this into the framework. This would mean that we could estimate everything at once, including surface reflectance spectra, light spectra, and camera spectral sensitivities all from only camera input images.

## Acknowledgment

This work was supported in part by Basic Science Research Program through the National Research Foundation of Korea (NRF) funded by the Ministry of Science, ICT & Future Planning (NRF-2013R1A1A1005065) and the Culture Technology (CT) Research & Development Program 2015 funded by the Ministry of Culture, Sports and Tourism (MCST) and Korea Creative Content Agency (KOCCA) (R2015040004).

## References

- [1] F. M. Abed, S. H. Amirshahi, and M. R. M. Abed. Reconstruction of reflectance data using an interpolation technique.

- JOSA A*, 26(3):613–624, 2009. 3
- [2] E.-W. Bai and Y. Liu. Least squares solutions of bilinear equations. *Systems & control letters*, 55(6):466–472, 2006. 4
- [3] K. Barnard, L. Martin, B. Funt, and A. Coath. A data set for color research. *Color Research & Application*, 27(3):147–151, 2002. 3, 5
- [4] C. Barnes, E. Shechtman, A. Finkelstein, and D. Goldman. Patchmatch: A randomized correspondence algorithm for structural image editing. *ACM Transactions on Graphics (Proc. SIGGRAPH)*, 28(3):24, 2009. 5
- [5] A. Chakrabarti and T. Zickler. Statistics of real-world hyperspectral images. In *CVPR*, pages 193–200, 2011. 2
- [6] C. Chi, H. Yoo, and M. Ben-Ezra. Multi-spectral imaging by optimized wide band illumination. *IJCV*, 86(2):140–151, 2010. 2
- [7] J. Cohen. Dependency of the spectral reflectance curves of the munsell color chips. *Psychonomic Science*, 1(1-12):369–370, 1964. 3
- [8] S. Cohen and C. Tomasi. *Systems of bilinear equations*. Tech. Rep. CS-TR-97-1588, Stanford University, 1997. 4
- [9] C. Collet, M. Louys, A. Oberto, and C. Bot. Markov model for multispectral image analysis: application to small magellanic cloud segmentation. In *ICIP*, pages 953–956, 2003. 2
- [10] P. Cotte and D. Dupraz. Spectral imaging of leonardo da vinci’s mona lisa: An authentic smile at 1523 dpi with additional infrared data. In *Proceedings of IS&T Archiving Conference*, pages 228–235, 2006. 2
- [11] H. Du, X. Tong, X. Cao, and S. Lin. A prism-based system for multispectral video acquisition. In *ICCV*, pages 175–182, 2009. 2
- [12] N. Gat. Imaging spectroscopy using tunable filters: a review. In *Proc. SPIE Wavelet Applications VII*, volume 4056, pages 50–64, 2000. 2
- [13] S. Han, I. Sato, T. Okabe, and Y. Sato. Fast spectral reflectance recovery using dlp projector. *IJCV*, 110(2):172–184, 2014. 2
- [14] S. Hordley, G. Finlayson, and P. Morovic. A multi-spectral image database and its application to image rendering across illumination. In *Proc. Int. Conf. on Image and Graphics*, 2004. 2
- [15] J. Jiang, D. Liu, J. Gu, and S. Susstrunk. What is the space of spectral sensitivity functions for digital color cameras? In *IEEE Workshop on Applications of Computer Vision (WACV)*, pages 168–179, 2013. 4, 5
- [16] D. B. Judd, D. L. MacAdam, G. Wyszecki, H. Budde, H. Condit, S. Henderson, and J. Simonds. Spectral distribution of typical daylight as a function of correlated color temperature. *JOSA A*, 54(8):1031–1040, 1964. 3
- [17] R. Kawakami, J. Wright, Y.-W. Tai, Y. Matsushita, M. Ben-Ezra, and K. Ikeuchi. High-resolution hyperspectral imaging via matrix factorization. In *CVPR*, pages 2329–2336, 2011. 2
- [18] R. Kawakami, H. Zhao, R. T. Tan, and K. Ikeuchi. Camera spectral sensitivity and white balance estimation from sky images. *IJCV*, 105(3):187–204, 2013. 3, 4, 5
- [19] S. J. Kim, F. Deng, and M. S. Brown. Visual enhancement of old documents with hyperspectral imaging. *Pattern Recognition*, 44(7):1461–1469, 2011. 2
- [20] S. J. Kim, H. Lin, L. Zheng, S. Susstrunk, S. Lin, and M. S. Brown. A new in-camera imaging model for color computer vision and its application. *TPAMI*, 34(12):2289–2302, 2012. 4
- [21] K. Lawrence, B. Park, W. Windham, and C. Mao. Calibration of a pushbroom hyperspectral imaging system for agricultural inspection. *Transactions of the ASAE*, 46(2):513–521, 2003. 2
- [22] H. Li, C.-W. Fu, and A. J. Hanson. Visualizing multiwavelength astrophysical data. *IEEE Transactions on Visualization and Computer Graphics*, 14(6):1555–1562, 2008. 2
- [23] M. A. Loghmari, M. S. Naceur, and M. R. Boussema. A spectral and spatial source separation of multispectral images. *IEEE Transactions on Geoscience and Remote Sensing*, 44(12):3659–3673, 2006. 2
- [24] R. Lu. Detection of bruises on apples using near-infrared hyperspectral imaging. *Transactions of the ASAE*, 46(2):523–530, 2003. 2
- [25] L. T. Maloney. Evaluation of linear models of surface spectral reflectance with small numbers of parameters. *JOSA A*, 3(10):1673–1683, 1986. 3
- [26] P. Morovic and G. D. Finlayson. Metamer-set-based approach to estimating surface reflectance from camera rgb. *JOSA A*, 23(8):1814–1822, 2006. 3
- [27] S. Nakariyakul and D. P. Casasent. Fast feature selection algorithm for poultry skin tumor detection in hyperspectral data. *Journal of Food Engineering*, 94(3):358–365, 2009. 2
- [28] R. M. Nguyen, D. K. Prasad, and M. S. Brown. Training-based spectral reconstruction from a single rgb image. In *ECCV*, pages 186–201, 2014. 3, 6, 7
- [29] R. Padoan, T. A. Steemers, M. Klein, B. Aalderink, and G. De Bruin. Quantitative hyperspectral imaging of historical documents: technique and applications. In *Proc. Int. Conf. on NDT of Art*, pages 445–446, 2008. 2
- [30] Z. Pan, G. Healey, M. Prasad, and B. Tromberg. Face recognition in hyperspectral images. *TPAMI*, 25(12):1552–1560, 2003. 2
- [31] J.-I. Park, M.-H. Lee, M. Grossberg, and S. K. Nayar. Multispectral imaging using multiplexed illumination. In *ICCV*, pages 1–8, 2007. 2
- [32] J. P. Parkkinen, J. Hallikainen, and T. Jaaskelainen. Characteristic spectra of munsell colors. *JOSA A*, 6(2):318–322, 1989. 3
- [33] D. Slater and G. Healey. What is the spectral dimensionality of illumination functions in outdoor scenes? In *CVPR*, pages 105–110, 1998. 3
- [34] E. Tola, V. Lepetit, and P. Fua. Daisy: An efficient dense descriptor applied to wide-baseline stereo. *TPAMI*, 32(5):815–830, 2010. 5
- [35] F. Yasuma, T. Mitsunaga, D. Iso, and S. K. Nayar. Generalized assorted pixel camera: postcapture control of resolution, dynamic range, and spectrum. *TIP*, 19(9):2241–2253, 2010. 2